Effect of oxide defect on photocatalytic properties of MSnO$_3$ (M = Ca, Sr, and Ba) photocatalysts

Huihui Li[*],[1], Yujun Gao[1], Daqiang Gao[*], Yuhua Wang

National & Local Joint Engineering Laboratory for Optical Conversion Materials and Technology, Key Laboratory of Special Function Materials and Structure Design, Ministry of Education, Lanzhou University, 222 South Tianshui Road, Lanzhou 730000, China

ARTICLE INFO

ABSTRACT

Since energy transfer to oxygen species is generally considered to be the critical step during the $O_2^{\cdot-}$-driven photocatalytic reaction, it is important to develop approaches to design the oxygen defects induced photocatalysts to improve the performance of oxygen chemisorption. Here we report that a new strategy of oxide defect controlled MSnO$_3$ catalyst is served to turn light into chemical energy by improving species chemisorption on the surface. CaSnO$_3$ with the Ca/Sn ratio of 2.7 (2.7-CaSnO$_3$) rich in oxygen vacancies exhibited a high photocurrent performance and an efficient photocatalytic activity. A superior photo efficiency is achieved for 2.7-CaSnO$_3$, which reduces 93.9% MB dyes within 30 min under 100 mW/cm^2 white LED light irradiation, approximately 3.2 times larger than its stoichiometric one. Under the same LED light irradiation, 577.4 μmol h^{-1} g^{-1} of H$_2$ and 62.0 μmol h^{-1} g^{-1} of O$_2$ are realized over 2.7-CaSnO$_3$. The chemisorption improved by oxygen defects in 2.7-CaSnO$_3$ enables the transfer of photogenerated electrons to oxygen species in space. Therefore, oxygen molecules are activated into superoxide radicals on the oxygen defect-rich MSnO$_3$ successfully. After more oxygen defects doping, the hydrogen evolution rate increases from 553.3 to 1152.7 μmol h^{-1} g^{-1}, while O$_2$ production rates increases from 62.0 to 129.1 μmol h^{-1} g^{-1}. The hydrogen reduction treatment further revealed that the enhancement of both hydrogen and oxygen evolution was realized by introducing more oxygen vacancies into 2.7-CaSnO$_3$.

1. Introduction

Photocatalytic reactions have been considered to be a promising process to substantially reduce the energy consumption. Solar energy can be harvested by semiconductor materials, which creates photo-excitation charge carriers to turn on chemical reactions on catalyst surface. Besides TiO$_2$ as the most photocatalyst, to effectively harness solar light, many novel photocatalysts such as Bi-based, Ag-based, In-based, Cu-containing and Co-containing photocatalysts have been also successfully developed [1–6]. However, the photon energy conversion with photocatalysts is far from practical use at the present stage [7]. A key reason for it is the limitation on the activation of charge migration from the interior to the surface of the semiconductor. To enable light-driven catalysis activation, the solar-to-chemical energy conversion process on oxide catalysts, whose efficiency relies on the energy coupling between photons, excitons and active species, should be certainly better harnessed. The solar harvesting responsible for photon-exciton energy conversion can be optimized by engineering band structures,

such as creation of defect states and formation of heterojunctions [8,9]. Recently, oxygen defect engineering for oxide semiconductors exhibits a positive role in the improvement of photocatalytic activity, such as oxygen defect induced WO$_3$, BiOCl, TiO$_2$, and Bi$_5$O$_7$Br [10–13]. Among various modification, the impurities or nonstoichiometric synthesis is one great possibility to enhance the photocatalytic activity, such as Cu$_x$In$_y$S, nonstoichiometric TiO$_2$, and Bi$_2$O$_2$CO$_3$ [14–16].

On the other hand, many active photocatalysts are perovskite-type compounds and have a general formula of ABX$_3$, such as SrTiO$_3$, SrSnO$_3$, and CaTiO$_3$ [17–19]. In their structure, transition metal ions on the B site reside in corner-sharing octahedra of X anions, and A-site cations have 12-fold coordination with X [20]. To date, many investigations have been carried out over perovskite surfaces, including oxidation of small molecules such as CO, hydrocarbons and NO$_x$, (photo)electrochemical splitting of H$_2$O, and reduction of CO$_2$ and N$_2$ [21–26]. The flexibility of the electronic and crystal structure and chemical versatility of ABO$_3$ perovskites can be used to establish design principles for highly active, selective, and stable catalysts [27].

Through careful materials design in perovskites, electronic structure can be tailored to the thermodynamic energies of a variety of reactions to minimize photocatalytic and chemical reaction barriers [28].

Herein, we demonstrate that defect engineering for alkaline earth metal stannate ($MSnO_3$, M = Ca, Sr, Ba) by nonstoichiometric synthesis. The chemisorption on oxygen defect site provides a channel for the delivery of photoexcited electrons to dioxygen species, as well as forms superoxide radicals in a chemisorption state upon receiving the electrons [10]. With identical oxidative capability to free superoxide radicals, the free superoxide radicals can efficiently react with the hole-charged substrate molecules located at the neighbor sites. Profiting from the chemisorption and activation of molecular oxygen on surface defects, the modified $MSnO_3$ exhibits enhanced photocatalytic activity.

2. Experimental

2.1. Preparation of MSnO₃ samples

In the present research, $MSnO_3$ powders were synthesized by hydrothermal reactions at 180 °C for 24 h followed by calcining at 700 °C for 6 h using various molar ratios of alkaline earth metal (Ca, Sr, and Ba) chloride and $SnCl_4·5H_2O$ as starting materials. The M/Sn atomic ratio was adjusted to 0.8, 1.0, 1.4, 1.7, 2.0, 2.3, 2.7, and 3.0. Typically, 0.5571 g $CaCl_2$ and 1.7571 g $SnCl_4·5H_2O$ were dissolved in 50 mL deionized water under vigorous stirring at room temperature. Subsequently, 15 mL of NaOH solution (4 mol/L) was added dropwise, vigorous stirring constantly for 1 h to get a uniform solution. Then, 65 mL of the above white turbid solution was transferred into a teflon-lined stainless steel autoclave with a capacity of 100 mL, maintained at 180 °C for 24 h. After cooling to the room temperature, the resulting powders with the Ca/Sn ratio of 1 were collected from the solution by centrifugation and washing, drying at 60 °C for 4 h, and then calcining at 700 °C for 6 h. To further study the performance, the designed $CaSnO_3$ powders were chosen and treated at 500 °C in H_2/N_2 for 2 h.

2.2. Characterization

X-ray diffraction (XRD) was carried out to observe the crystallinity of samples on a Bruker D2 PHASER diffractometer with Cu Kα radiation source. The scanning electron microscope images were obtained by JSM-7500 F instrument. Transmission electron microscopy (TEM) images were taken by a F30 S-TWIN electron microscope (TecnaiG2, FEI Company). X-ray photoelectron spectroscopy (XPS) and ultraviolet photoelectron spectroscopy (UPS) were performed on a PHI-5702 instrument from Thermo Fisher Scientific, USA. Standard C 1 s peak was used as a reference for correcting the shifts. The ultraviolet-visible (UV–vis) absorption spectra were obtained by using an UV–vis spectrophotometer (PE Lambda 950) with an integrating sphere attachment in the range of 200 to 800 nm and with $BaSO_4$ as reflectance standard. Photoluminescence (PL) spectra measurements were performed using a FLS-920 T fluorescence spectrophotometer with the excitation wavelength of 350 nm. Fourier transform infrared (FT-IR) spectra were recorded using a VERTEX 70 V/80 V spectrometer (Bruker, Germany) by means of the KBr pellet technique. The MS were obtained with Bruker Daltonics esquire6000 mass instrument (ESI) for the identification of oxidative degradation intermediates in the dye solution. Mott-Schottky plots were obtained with an electrochemical work-station (CHI 660E). Zeta potential of 2.7-$CaSnO_3$ powder was measured by a Zeta Potential Analyzer (Zetasizer Nano S90, Malvern). The initial pH value of RhB, MB, and phenol aqueous solution was indicated by a pH meter (PHS-25, INESA).

2.3. Photocatalytic experiments

2.3.1. Degradation of MB dyes solution

The photocatalytic activity of $MSnO_3$ was evaluated by the degradation of MB aqueous solutions under white LED light irradiation in a photochemical reaction apparatus (365–940 nm, 100 mW/cm², CEL-LAB100E, CEAULIGHT). In a typical experiment, 20 mg of the sample was added to 50 mL of MB aqueous solution (10 mg/L). Prior to irradiation, the suspensions were stirred in dark for 30 min to reach adsorption/desorption equilibrium. At certain irradiation time intervals, 4 mL aliquots were sampled and centrifuged to remove the particles. The filtrates were analyzed by measuring the maximum absorption peak (664 nm for MB solution) using a LG-722SP spectrophotometer. The active species generated in the photocatalytic system could be detected through trapping by iso-Propyl alcohol (IPA), benzoquinone (BQ), and ammonium oxalate (AO). To detect generation of reactive species, electron paramagnetic resonance (EPR) signals of radical spin-trapped by 5, 5-dimethyl-1-pyrroline-*N*-oxide (DMPO) were collected by a Bruker A300-9.5/12 at 100 kHz field modulation in the standard TE102 regular cavity operating in the X-band at 9.45 GHz. Besides MB dye, CV (crystal violet), RhB, MO, and phenol were also used as a target. For Cr (VI) photocatalytic reduction, 20 mg of photocatalyst was dispersed in 50 mL of Cr (VI) containing aqueous solution (20 mg/L) with 5 mL of ethanol using as a hole scavenger. After 40 min stirring in the dark to reach the adsorption-desorption equilibrium, the photocatalytic reaction was initiated by the same white LED light. The concentration of Cr (VI) was monitored by UV–vis spectrophotometer.

2.3.2. H₂ and O₂ generation

Photocatalytic reactions were performed in a closed quartz tube under vacuum conditions. The as-prepared sample (15 mg) was dispersed in distilled water by a magnetic stirring and irradiated by the same 100 W LED lamp. H_2 generation experiment was performed in a 45 mL C_2H_5OH aqueous solution (11 vol.%), while O_2 evolution reaction was taken out in a 55 mL $AgNO_3$ aqueous solution (10 mM), respectively, both of two reactions were carried out without any cocatalyst. The amounts of produced H_2 and O_2 were determined by a calibrated Varian GC-3380 Gas Chromatograph equipped with a thermal conductivity detector, using nitrogen as the carrier gas.

2.4. Photoelectrochemical measurements

Photocurrent measurements were carried out on an electrochemical workstation (CS 310, Wuhan Corrtest Instrument Co. Ltd.) in a standard three electrode system, with the as-prepared samples (effective area is 1 cm²) as working electrodes, a platinum foil as the counter electrode and an Ag/AgCl (saturated KCl) electrode as a reference electrode. The working electrodes were suspended into Na_2SO_4 (0.1 mol L^{-1}) aqueous solution with a 300 W Xe arc lamp equipped with a UVIRCUT filter (420–780 nm) regarded as the visible light source. All measurements are carried out with light ON-OFF switches of 6 s at a constant potential of 0.1 V to the working electrode. The electrochemical impedance spectroscopies (EIS) are performed at the open circuit potential. The frequency is ranging from 0.01 Hz to 100,000 Hz and the amplitude of the sinusoidal wave is 10 mV.

3. Results and discussion

Generating oxygen defect by a nonstoichiometric synthesis was carried out to improve the photocatalytic activity. In the present research, alkaline earth metal stannate ($MSnO_3$) powders were synthesized with various M/Sn atomic ratios. To investigate the structure and morphology, XRD patterns and TEM images were determined. The XRD patterns of stoichiometric $CaSnO_3$, $SrSnO_3$, $BaSnO_3$ and various M/Sn ratio photocatalysts are shown in Fig. 1. As can be seen from Fig. 1A(a–b), all the diffraction peaks of the stoichiometric $CaSnO_3$ can be exactly indexed as the orthorhombic structure (JCPDS no.77-1797). With increasing the Ca/Sn atomic ratio, the intensity of three main peaks at 22.4°, 31.9°, and 45.8° become weaker (Fig. S1a). There is no impurity peak in the $CaSnO_3$ with a Ca/Sn ratio lower than M/Sn
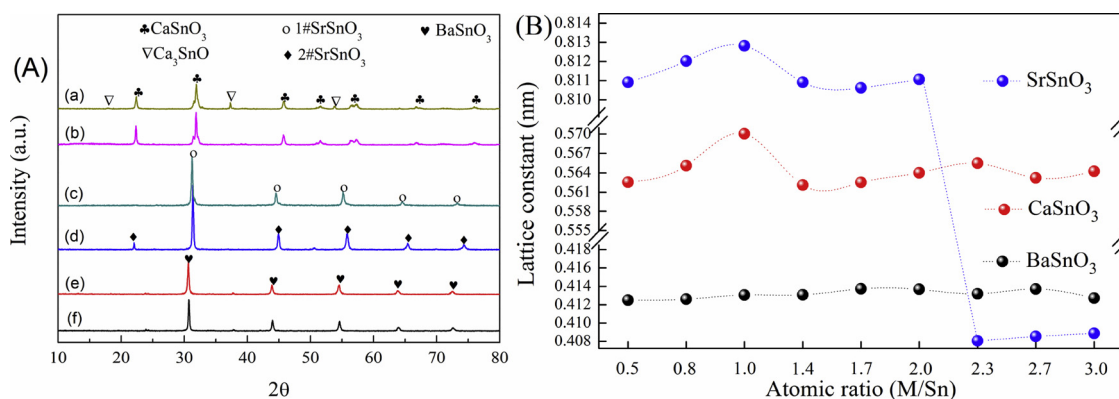
Fig. 1. (A) XRD patterns of (a) 2.7- and (b) 1.0- CaSnO$_3$, (c) 2.3- and (d) 1.0- SrSnO$_3$, (e) 1.7- and (f) 1.0- BaSnO$_3$ samples. (B) The lattice constants *vis* M/Sn atomic ratio of the prepared samples.

atomic ratios of 1.7, whereas the as-prepared samples with a higher Ca/Sn ratio (> 1.7) exhibit the extra diffraction peak of Ca$_3$SnO with a cubic structure (JCPDS no.83-1863) at 17.9°, 37.3° and 53.8° (Fig. S1a). The peak intensities of Ca$_3$SnO samples gradually increase with the increase in Ca/Sn ratio (Fig. S1a). As shown in Fig. S1b, the SrSnO$_3$ samples with the Sr/Sn ratio lower than 1.4 are of a cubic structure with *a* value of 8.068 nm (JCPDS no.22-1442). With increasing the Sr/Sn ratio larger than 1.7, besides the SrSnO$_3$ phase, the Sr$_2$SnO$_4$ (JCPDS no.24-1241) phase with a tetragonal structure can be observed. Then, after increases the Sr/Sn ratio to 2.3, the peak at 2θ = 21.9° disappears and the samples show the SrSnO$_3$ phase (JCPDS no.02-1448) with cubic structure (a = 4.033 nm). Therefore, the SrSnO$_3$ samples with the Sr/Sn ratio of 1.0 or 2.3 are of the same cubic structure but the different *a* value (Fig. 1A(c–d)). As shown in Fig. 1A(e) and 1 A(f), the 1.0-BaSnO$_3$ and 1.7-BaSnO$_3$ present the BaSnO$_3$ phase with a cubic structure (JCPDS no.22-1442). After modification, no impurity peak appears in the XRD patterns of other BaSnO$_3$ (Fig. S1c).

These results suggest that the formation of lattice defect or change in the valence state of metal ion occurs for the charge compensation. M deficient alkaline earth metal stannate such as $(M_{1-x}\square_x)Sn(O_{3-x}\square_x)$ or mixed valence alkaline earth metal stannate such as $(M_{1-x}\square_x)$ $(Sn_{1-2x}^{4+}Sn_{2x}^{2+})(O_{3-2x}\square_{2x})$ might be formed when M/Sn atomic ratio is smaller than 1.0, whereas when M/Sn atomic ratio is greater than 1, Sn deficient alkaline earth metal stannate such as $M(Sn_{1-x}\square_x)(O_{3-2x}\square_{2x})$ might be formed, where $\square$ is the vacancy. Fig. 1B shows the lattice constant of the samples with variation in M/Sn atomic ratios. It can also be seen that the lattice constant increases with an increase in M/Sn (M = Ca, Sr) atomic ratio up to 1.0 and then decreases by further increase in M/Sn atomic ratio. The lattice constant decreases sharply when the Sr/Sn atomic ratio increases to the value of 2.0, which might be related to the formation of impurity phase.

Fig. 2 shows TEM images of 2.7-CaSnO$_3$, 2.3-SrSnO$_3$, and 1.7-BaSnO$_3$ photocatalyst. The 2.7-CaSnO$_3$ sample presents a cubic structure with a particle size of about 1.45 μm, while the 2.3-SrSnO$_3$ rods has an average length of ∼0.95 μm and an average diameter of ∼0.16 μm. The 1.7-BaSnO$_3$ also shows a rod structure but with a larger average length (∼1.78 μm) and diameter (∼1.18 μm). Furthermore, the morphology of as-prepared samples is also observed by SEM measurement. As shown in Fig. S2, the morphology structures of MSnO$_3$ are almost unchanged. The 2.7-CaSnO$_3$ crystalline particles have a size between 0.5 and 2 μm, smaller than that of 1.0-CaSnO$_3$ (1–4 μm), in Fig. S2a-b. As shown in Fig. S2c-d, compares with stoichiometric SrSnO$_3$, the modified one (Sr/Sn = 2.3) crystalline particles also exhibits rod-like shape with the diameter between 3.62 and 19.78 μm and the length between 5.67 and 32.03 μm. However, the morphology and particle size of modified BaSnO$_3$ are similar to those of stoichiometric one, about 7 μm in diameter and 30 μm in length (Fig. S2e-f). After M/Sn ratio modification, the particle sizes of CaSnO$_3$ decrease, however, those of SrSnO$_3$ or BaSnO$_3$ increase. It is worth noting that only CaSnO$_3$ exhibits the similar particle size in both TEM and SEM results, while the size difference is dramatic large between two morphology analysis results of SrSnO$_3$ or BaSnO$_3$.

The M and Sn atoms with low coordination numbers provide sites for oxygen species chemisorption. To investigate the chemisorption, XPS is employed to characterize the oxygen atoms involve in MSnO$_3$ (Fig. 3). All atoms are determined by high-resolution XPS calibrated with the reference carbon at 284.6 eV. In O1 s XPS spectrum (Fig. 3A), the peaks at ca. 529 eV for all samples are attributed to the lattice oxygen ubiquitously in oxide semiconductors [29]. The additional peak at ca. 531 eV is arising from the oxygen species chemisorbed at oxygen vacancies, another O 1 s peak at ca. 533 eV is derived from the hydroxyl group [30,31]. Compare with stoichiometric CaSnO$_3$, the intensity of the O 1 s peak at 531.2 eV is obviously enhanced while that of 529.6 eV peak is weaken in the modified one (Ca/Sn = 2.7) (Fig. 3A(a–b)),
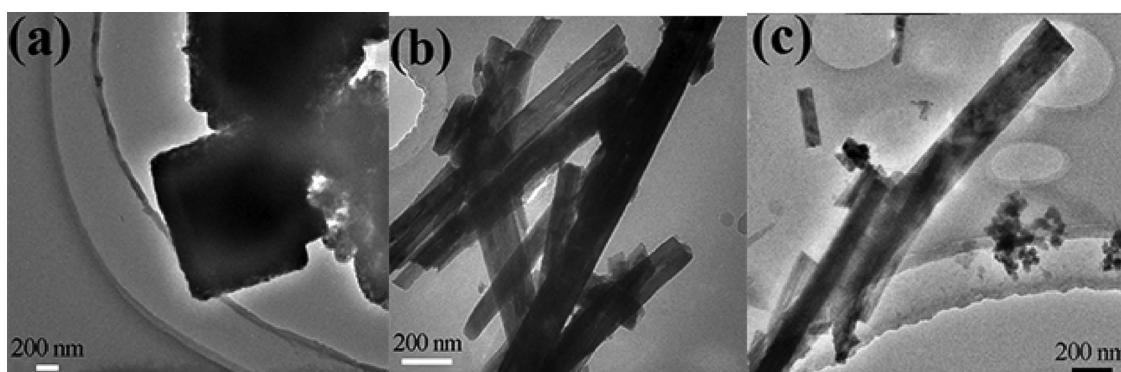

Fig. 2. TEM images of (a) 2.7-CaSnO$_3$, (b) 2.3-SrSnO$_3$, and (c) 1.7-BaSnO$_3$ samples.
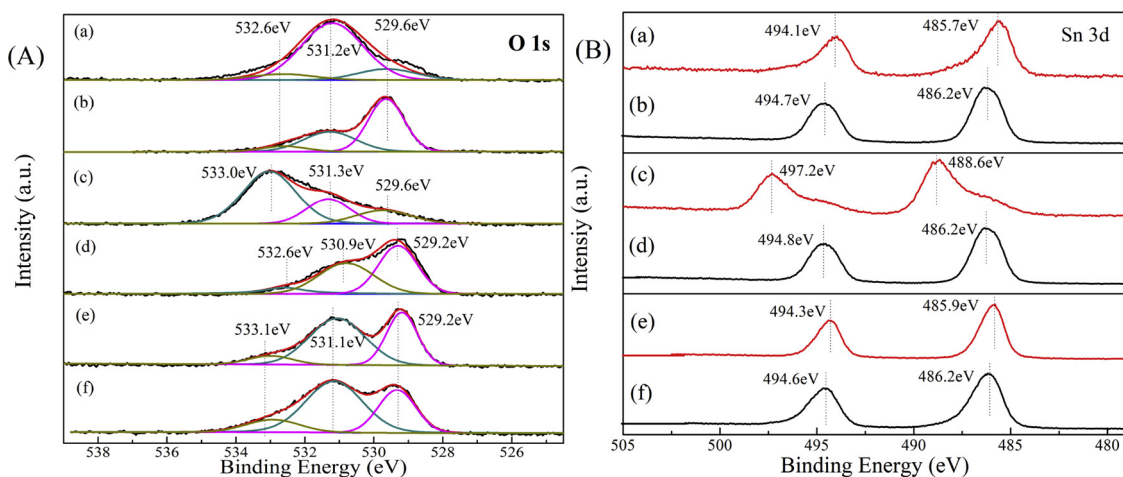
Fig. 3. (A) O1 s and (B) Sn 3d XPS of (a) 2.7- and (b) 1.0- CaSnO$_3$, (c) 2.3- and (d) 1.0- SrSnO$_3$, (e) 1.7- and (f) 1.0- BaSnO$_3$ samples.

demonstrate the increasing of the oxygen vacancy or defect and the decreasing of the lattice oxygen in the CaSnO$_3$. The peak at ca. 533 eV is almost unchanged. The O 1 s peaks at 529.2, 530.9, and 532.6 eV for 1.0-SrSnO$_3$ shift to 529.6, 531.3, and 533.0 eV for 2.3-SrSnO$_3$, with the intensity change (Fig. 3A(c–d)). The lattice oxygen of 2.3-SrSnO$_3$ notably reduce, the chemisorbed oxygen increase, indicating crystal internal has appeared the large evolution, such as oxygen vacancy or chemisorbed oxygen species. Besides, the hydroxyl groups are also improved according to the increase of the peak at 533.0 eV in 2.3-SrSnO$_3$. However, as shown in Fig. 3A(e–f), no obvious changes are observed between the two mentioned BaSnO$_3$ samples.

In Sn 3d XPS spectrum (Fig. 3A), the peaks at ca. 486 and 495 eV for all samples are attributed to Sn 3d$_{5/2}$ and Sn 3d$_{3/2}$, respectively [32]. After nonstoichiometric synthesis, Sn 3d peaks in both CaSnO$_3$ and BaSnO$_3$ shift to the lower binding energy, while those in SrSnO$_3$ shift to the higher binding energy. XRD result presents that there is a crystal phase transition in the modified SrSnO$_3$ (Sr/Sn = 2.3). Therefore, the changes occurred in both the chemical environment of SrSnO$_3$ the binding energy of Sr, Sn, and O, also suggesting vacancy and/or defects.

As shown in Fig. S3a, Ca 2p peaks at 346.1 (Ca 2p$_{3/2}$) and 349.6 (Ca 2p$_{1/2}$) eV for stoichiometric CaSnO$_3$ shift to 346.7 and 350.2 eV for CaSnO$_3$ with Ca/Sn ratio of 2.7. As shown in the above XRD patterns results, the sample with the Ca/Sn ratio of 2.7 contains both CaSnO$_3$ and Ca$_3$SnO phases. The balanced charge for Ca$_3$SnO would be Ca$_3^{2+}$ Sn^{4-} O^{2-} and exist some Ca, Sn, O vacancy defects inside the sample. The Sr 3d$_{5/2}$ and Sr 3d$_{3/2}$ binding energies of 1.0-SrSnO$_3$ sample are 132.5 and 134.2 eV, while those are 132.7 and 134.4 eV in 2.3-SrSnO$_3$ (Fig. S3b). The additional peak at 136.1 eV in the 2.3-SrSnO$_3$ is owing to the crystal phase transition [33]. The Ba 3d$_{5/2}$ and Ba 3d$_{3/2}$ binding energies of 1.0- and 1.7- BaSnO$_3$ samples are similarly located at 779.1 and 794.5 eV, respectively (Fig. S3c). In short, for MSnO$_3$ compounds, only the element of M site is different, with the increasing of M/Sn and M radius (Ca^{2+} < Sr^{2+} < Ba^{2+}), the XPS peaks of Ca and Sr do change, including the peak shift and intensity. But no change can be observed in the Ba XPS peaks. However, for the 1.7-CaSnO$_3$, another Ca-based perovskite material, which has the same M/Sn ratio as 1.7-BaSnO$_3$, Ca 2p3/2 peak and Ca 2p1/2 peak shift to 346.6 and 350.1 eV respectively (Fig. S3d). Compared with Ca- stannate, it is difficult for Ba-stannate formation with high Ba/Sn molar ratio owing to the high atomic radius of Ba [34]. The similar phenomenon was also observed in ACoO$_3$ (A = La, Ba, Sr and Ce), Sn contained Fe$_2$O$_3$ [34,35].

Taking 2.7-CaSnO$_3$ as an example, the crystal structural information can be shown as Fig. 4A. As shown in the above O 1 s XPS, the increase intensity of peak at 531.2 eV, arising from the chemisorbed oxygen species. It also indicates that the oxygen vacancies are stabilized by the adsorbed oxygen species [10]. Therefore, the O$_2$ molecule can be

chemisorbed at the oxygen vacancy of 2.7-CaSnO$_3$ (Fig. 4B). The chemisorption benefits the electron transfer from unsaturated Ca or Sn site to O$_2$ species. However, there is almost no site on the 1.0-CaSnO$_3$ surface to chemisorb O$_2$ (Fig. 4C). Thus, owing to the strong coupling between defective 2.7-CaSnO$_3$ and O$_2$, energy transfer from excitons to O$_2$ species can be realized under proper light irradiation.

The reactive oxygen species will be formed after O$_2$ molecule accepting an additional electron during semiconductor photoexcitation. To trace the O$_2$ and further study the photoinduced electrons utilization, the ESR test with DMPO, a typical spin-trapping agent for O$_2^{·-}$, was employed to examine the 2.7-CaSnO$_3$ sample in methanol [36]. For comparison, 1.0-CaSnO$_3$ sample was also studied under the same condition. As shown in Fig. 5A, almost no O$_2^{·-}$ was produced over 1.0-CaSnO$_3$ catalyst. However, the ESR signals with a 0.6:0.8:1:1:0.8:0.7 sextuple pattern are detected when the reaction is carried out for 2.7-CaSnO$_3$ photocatalyst. The strong peak intensity of 2.7-CaSnO$_3$ in the DMPO-O$_2^{·-}$ species demonstrates that the CaSnO$_3$ with oxygen vacancies can significantly better activate O$_2$ into O$_2^{··}$ species through electron transfer. It suggests that the chemisorption indeed can facilitate the energy transfer from excitons to O$_2$ species.

Defect engineering creates oxygen vacancies on oxide surface which can provide unsaturated sites for molecular adsorption [10]. To study the adsorption ability, the adsorption experiment is carried out over the as-prepared MSnO$_3$ photocatalysts in the dark. The results are shown in Fig. 5B and more in detail in Fig. S5a. After persistently stirring in the dark for 60 min, 96.2, 79.3, 95.3, 81.8, 96.3, 96.2% of MB are detected in the solution with 1.0- or 2.7-CaSnO$_3$, 1.0- or 2.3-SrSnO$_3$, and 1.0- or 1.7-BaSnO$_3$ photocatalyst, respectively. Then, the BET specific surface area are 4.55, 2.74, and 0.30 m^2/g for 2.7-CaSnO$_3$, 2.3-SrSnO$_3$, and 1.7-BaSnO$_3$, and 0.33, 0.36, and 0.39 m^2/g for 1.0-CaSnO$_3$, 1.0-SrSnO$_3$, and 1.0-BaSnO$_3$, respectively. It shows that there are no significant changes between nonstoichiometric and stoichiometric MSnO$_3$, suggesting that simply physical adsorption is not the only origin for the MB adsorption. Similar to the O$_2$ chemisorbed at the surface of 2.7-CaSnO$_3$ in Fig. 4B, the chemisorption on nonstoichiometric MSnO$_3$ can improve the MB adsorption which will be a good supplement for the efficient photocatalytic reaction.

Fig. S5A shows the time dependent concentration of MB dye aqueous solution in the presence of different stannate photocatalysts in the dark. Dramatically adsorption compared to the stoichiometric CaSnO$_3$ and SrSnO$_3$ reveals that besides the physical adsorption on 1.0-CaSnO$_3$ (3.8%), 1.0-SrSnO$_3$ (4.7%), and 1.0-BaSnO$_3$ (3.7%), the additional chemisorption for MB onto the surface of 2.7-CaSnO$_3$, 2.3-SrSnO$_3$ and 1.7-BaSnO$_3$ occurred in the concentration range from 16.9 (2.7-CaSnO$_3$), 13.5 (2.3-SrSnO$_3$) to 0.1% (1.7-BaSnO$_3$), for the reason that some of oxygen defect is introduced.
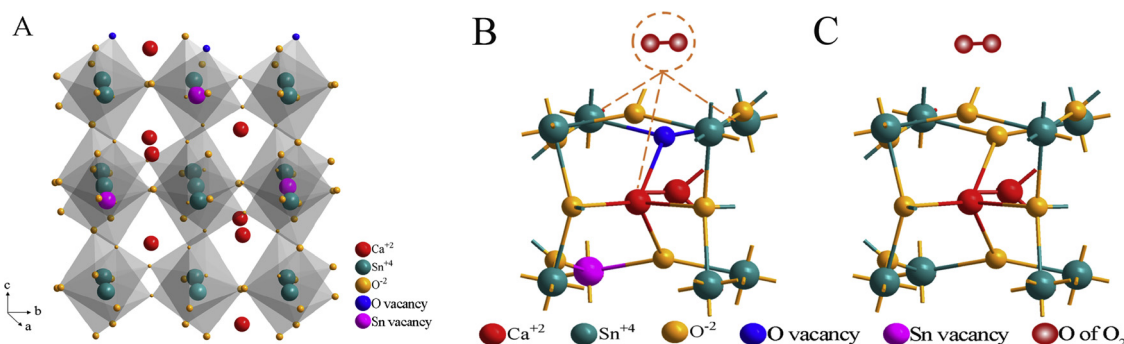
Fig. 4. Crystal models for (A) the locations of oxygen vacancies in 2.7-CaSnO$_3$ lattice; (B) the O$_2$ chemisorbed at unsaturated Ca or Sn site of 2.7-CaSnO$_3$; and (C) the O$_2$ adsorbed at the surface of 1.0-CaSnO$_3$.

In order to further verify the adsorption mechanism of MB dyes on photocatalyst surface, FTIR spectroscopy characterization of stannate photocatalyst surface after 40 min immersion in MB dyes aqueous solution in the dark was performed and shown in Fig. S5B. For both two CaSnO$_3$ sample, the peaks at about 3336, 3228, 1631.8 cm^{-1} are owing to the bending mode of the adsorbed water, while peaks at 519 and 454 cm^{-1} represent the characteristics of Sn-O and Ca-O vibrations. The bands located at 875 and 1450 cm^{-1} are assigned to carbonate vibrations [37,38], and vibrational bands of CO$_2$ are also observed, owing to the MB degradation in the evaluation process. It also exhibits peak at 1795 cm^{-1} corresponding to carbonyl groups on the surface of samples. The band located at 1449 cm^{-1} ascribed to the aromatic ring vibrations and 1105 cm^{-1} assigned to the C−S−C vibration in MB molecular are detected, suggesting the adsorption of MB molecular on photocatalyst surface. In addition, the peaks at 1793, 1450, and 1100 cm^{-1} in 1.0-CaSnO$_3$ shift to 1795, 1448, and 1105 cm^{-1} in 2.7-CaSnO$_3$, respectively, due to MB adsorption by electrostatic forces on the negative charge surface of 2.7-CaSnO$_3$.

Fig. S5C-S5E show the FTIR spectrum of the as-prepared stannate samples after white LED light driven MB dyes photocatalytic degradation. Since all the samples was evaluated after MB degradation reaction, the peaks corresponding to carbonate vibrations could be observed. For CaSnO$_3$, the bands below 700 cm^{-1} represent the characteristics of Ca-O and Sn-O vibrations [39]. A band at 643 cm^{-1} is assigned to the stretching mode of Sn-O, while a mode at 503 cm^{-1} is ascribed to SnO$_6$ vibration [39]. Then, for SrSnO$_3$, both two samples show similar spectral features, the most characteristic feature being the high-intensity infrared absorption band at 644 cm^{-1} which corresponds to the vibrations of the stannate group (SnO$_3^{2-}$) [40]. Moreover, no bands from the precursor SrSn(OH)$_6$ or other impurities can be observed. For

BaSnO$_3$, the peak at 467 cm^{-1} can be related to Ba-O band, and the characteristic band of the barium stannate appears at 646 cm^{-1} [41]. Comparison result is that the peaks assigned to Sn-O and Ca-O vibrations in 1.0-CaSnO$_3$ shift to lower wavenumber region in 2.7-CaSnO$_3$. There is a same phenomenon in which the characteristic peaks shift to lower wavenumber region in SrSnO$_3$ after introducing defects. However, no obvious difference can be observed between 1.0-BaSnO$_3$ and 1.7-BaSnO$_3$. The difference between modified MSnO$_3$ and stoichiometry one in IR study is well agree with the results in the above XPS investigation, indicating that the defects also exist in the surface of modified samples.

Thanks to the efficient charge transfer to O$_2$, the formed free superoxide radicals will efficiently drive the O$_2$-pariciping catalytic reactions. To evaluate the catalytic performances, the experiments of hydrogen evolution, oxygen production, and MB degradation in which active oxygen species plays a critical role are carried out.

First, the degradation of MB solution has been performed to estimate the photocatalytic ability of MSnO$_3$ under white LED lamp, as shown in Fig. S4. The value of the rate constant k, which is equal to the corresponding slope of the degradation line, is used to investigate the photocatalytic performance [42]. The photocatalytic activities of different BaSnO$_3$ are the same whereas all of the CaSnO$_3$ and SrSnO$_3$ photocatalysts exhibit much higher photocatalytic activity than the BaSnO$_3$ samples under white LED lamp irradiation. For CaSnO$_3$ or SrSnO$_3$, the photocatalytic activity is improved gradually with the M/Sn ratio increasing. When the Ca/Sn ratio reaches 2.7, the as-prepared CaSnO$_3$ photocatalyst exhibits the highest photocatalytic activity. The rate constant k is 0.0239 min^{-1} and is almost 4.0 times as high as that of CaSnO$_3$ with the Ca/Sn ratio of 1. For SrSnO$_3$ photocatalyst, the best Sr/Sn ratio is 2.3. However, further increasing the Ca/Sn or Sr/Sn ratio,
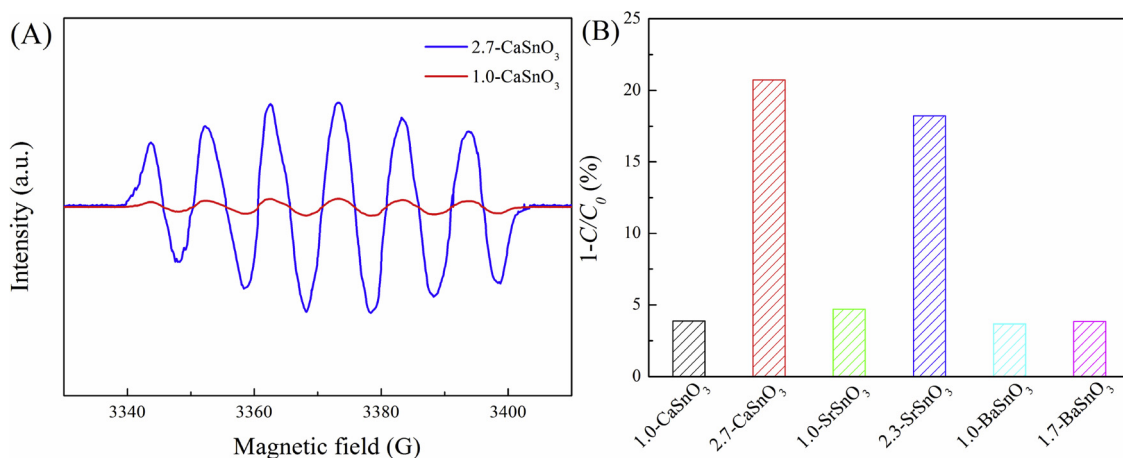

Fig. 5. (A) ESR detection of superoxide radicals using a DMPO spin-trapping agent; (B) The decolorization of MB dyes over different MSnO$_3$ in the dark after the balance between adsorption and desorption is achieved.
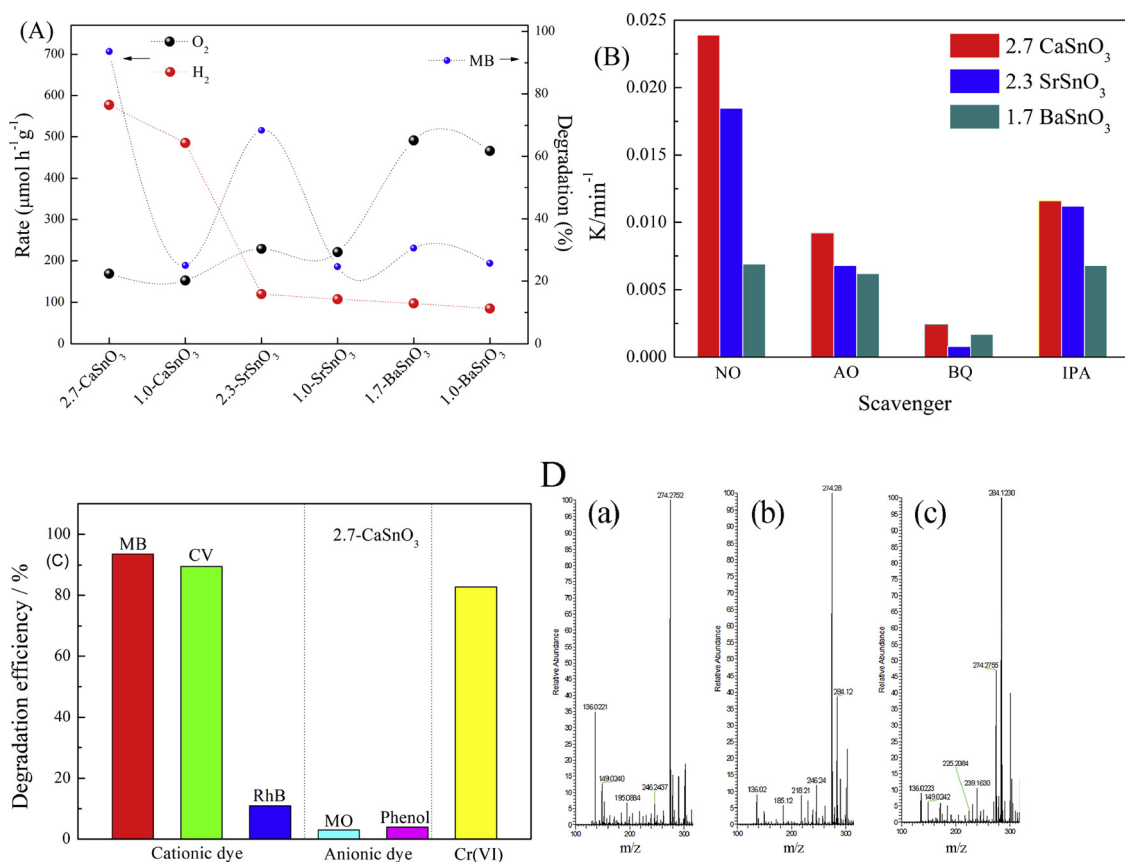
Fig. 6. (A) Photocatalytic hydrogen or oxygen evolution rate and MB decolorization over various MSnO₃; (B) Photogenerated carriers trapping in the system of photocatalytic degradation of MB over 2.7-CaSnO₃, 2.3-SrSnO₃, and 1.7-CaSnO₃. NO: nothing added; AO: ammonium oxalate added; BQ: benzoquinone added; IPA: iso-Propyl alcohol added. (C) Photocatalytic performance of 2.7-CaSnO₃ on cationic and anionic dyes degradation and Cr (VI) reduction under white LED light irradiation. (D) Positive mass spectra of the major production after photocatalytic MB degradation over (a) 2.7-CaSnO₃, (b) 1.0-CaSnO₃ and (c) MB original solution.

the degradation rates will decrease gradually. As shown in Fig. 6A, the 2.7-CaSnO₃ shows excellent photocatalytic and the photocatalytic activity is higher than that of the 2.3-SrSnO₃. After 30 min irradiation, the 2.7-CaSnO₃ photocatalyst can degrade MB by 93.9%, while it degrades 68.3% of MB over 2.3-SrSnO₃. It is notable that the Ba/Sn ratio modification does not obviously enhance the photocatalytic activity of BaSnO₃, all BaSnO₃ samples spend 30 min on degrading MB ca. 27% under the same white LED lamp irradiation.

Then, in photocatalytic H_2 and O_2 evolution reactions, easily oxidizable reagent C_2H_5OH and reducible reagent $AgNO_3$ were used as the electron donor and electron acceptor, respectively, to consume photogenerated holes in the valence band and photogenerated electrons in the conduction band. The dependence of photocatalytic H_2 and O_2 evolution on the different MSnO₃ is investigated under white LED light irradiation. First, the production rates of H_2 evolution for 1.0-CaSnO₃, 1.0-SrSnO₃, and 1.0-BaSnO₃ are about 485.2, 107.6, and 85.2 μmol h^{-1} g^{-1}, while those of O_2 evolution are about 56.0, 81.0, and 171.0 μmol h^{-1} g^{-1}, respectively. From Fig. 6A, with the increase of the ionic radius in the A site, the H_2 evolution rates for the CaSnO₃, SrSnO₃, and BaSnO₃ photocatalyst show a periodic trend, while the O_2 evolution rates also show a periodic trend but with opposite order. The order of the photocatalytic activities of H_2 evolution is CaSnO₃ > SrSnO₃ > BaSnO₃, while that of O_2 evolution is CaSnO₃ < SrSnO₃ < BaSnO₃. The production rates of H_2 evolution for 2.7-CaSnO₃, 2.3-SrSnO₃, and 1.7-BaSnO₃ are about 577.4, 120.0, and 97.4 μmol h^{-1} g^{-1}, those of O_2 evolution are about 62.0, 84.0, and 180.3 μmol h^{-1} g^{-1}, respectively. The rates of H_2 and O_2 evolution increase with increase the M/Sn ratio to 2.7, 2.3, and 1.7 for CaSnO₃, SrSnO₃, and BaSnO₃, respectively, which should be attributed to the

marked increase of the active sites. The as-prepared 2.7-CaSnO₃ photocatalyst shows higher photocatalytic performance than many other stannate based or alkaline earth metal contained photocatalyst, as shown in Table S1.

To detect the main active species in the photocatalytic process, the trapping experiments of radicals and holes are performed under white LED lamp irradiation in the presence of BQ ($O_2^{\cdot-}$ scavenger), AO (h^+ scavenger) and IPA (·OH scavenger) respectively [43]. As shown in Fig. 6B, in the CaSnO₃ and SrSnO₃ system, the addition of a scavenger of radicals can obviously bring damage on MB degradation. The photocatalytic activity could be greatly suppressed by the addition of a scavenger for $O_2^{\cdot-}$ (BQ), suggesting that the $O_2^{\cdot-}$ radicals are the main active species. In the BaSnO₃ system, the photocatalytic activity is also greatly prevented by the BQ, indicating the $O_2^{\cdot-}$ radicals play an important role in photocatalytic reaction.

To assess the photocatalytic performance of 2.7-CaSnO₃ on degradation dyes with different charges, cationic MB, CV, RhB, and anionic MO, phenol dyes were chosen for target molecules [44–46]. As shown in Fig. 6C, after 30 min white LED light irradiation, the degradation ratio of 2.7-CaSnO₃ for MB, CV, RhB, MO, phenol dyes are 93.9, 89.6, 10.7, 3.3, 4.5% respectively. Besides RhB, the cationic MB and CV were almost adsorbed and degraded completely, in contrast, trace MO or phenol was removed from the aqueous solution. The results suggest that the dye degradation greatly depended on the type of charge of relevant organics. The dye moleculars containing more aromatic or heterocyclic rings have less adsorption capacity owing to the higher of the steric hindrance effects of substituents [44]. The difficulty for the large molecule RhB to be adsorbed on the surface of 2.7-CaSnO₃ results in the low degradation rate [45]. The selectivity on photocatalytic dyes

Table 1
Photocatalytic performance of CaSnO$_3$ for different photocatalytic reaction before and after oxygen vacancies induced.

Samples	Product (µmol/h/g)		Cationic dye (%, 30 min)			Anionic dye (%, 30 min)		Cr(VI) (%, 2 h)
	H$_2$	O$_2$	MB	CV	RhB	MO	Phenol	
2.7-CaSnO$_3$	577.4	62.0	93.9	89.6	10.7	3.3	4.5	87.2
1.0-CaSnO$_3$	485.2	56.0	25.0	23.6	5.2	2.1	2.6	55.4

degradation indicates that the charge of 2.7-CaSnO$_3$ should be negative after introducing oxygen defects. The initial pH value of RhB, MB, and phenol aqueous solution are 7.3, 7.6 and 7.9, respectively. As shown in Fig. S10, the 2.7-CaSnO$_3$ particles have negative zeta potential in an alkaline environment. Thus, it cannot accommodate anionic dye molecules. In short, the degradation performance greatly depends on the contaminant charges due to the negatively charged photocatalyst surface, which greatly influences the adsorption of the target contaminants to the catalyst active sites. The adjustment of the surface electrochemistry behavior of MSnO$_3$ for target molecule will greatly increase its degradation efficiency. In addition, the photocatalytic reduction of Cr (VI) over 2.7-CaSnO$_3$ was also carried out in aqueous solution. Fig. 6C and Table 1 reveal that the Cr (VI) reduction efficiency increases from 55.4% on 1.0-CaSnO$_3$ to 87.2% on 2.7-CaSnO$_3$ after 120 min of white LED light irradiation. The degradation rate of 87.2% for 2.7-CaSnO$_3$ is about 1.6 times higher than the stoichiometric one. It also suggests that the enhancement of the surface negative charge on CaSnO$_3$ after oxygen vacancies formation, since the negative charges on the catalyst surface supplying a large amount of adsorption sites for Cr (VI) cation [47].

The MS measurement was carried out to study the degradation intermediate products, as shown in Fig. 6D. According to the slow self-degradation of MB dye, not only the characteristic peak of m/z 284 but also the peaks corresponding to the homologues of MB can be observed clearly in MB original solution (Fig. 6D(c)). The different de-methylated products of the MB dye observed in MS are: C$_{14}$H$_{15}$N$_3$OS (m/z = 274), Azure-C (m/z = 239), thionin (m/z = 225), 6-Aminobenzothiazole (m/z = 149), and benzothiazole (m/z = 136) [48,49]. Compared with positive mass spectra peaks of the parent molecule, the cationic MB of m/z 284 becomes much lower intensity over 1.0-CaSnO$_3$, while the m/z 284 indeed vanishes after white LED light irradiation for 30 min in the presence of 2.7-CaSnO$_3$. The 1.0-CaSnO$_3$ photocatalyst can produce the following stable intermediates with m/z values of 274, 246 (C$_{12}$H$_{11}$N$_3$OS), 218 (C$_8$H$_{11}$N), 185 (C$_8$H$_{11}$NO$_2$), and 136, while peaks at 274, 246, 195 (C$_8$H$_6$O$_6$), 149 (C$_6$H$_6$O$_4$), and 136 amu can be observed over 2.7-CaSnO$_3$ [48,49].

After that, the degradation pathway is proposed, as shown in Scheme S1. The active radicals generated over CaSnO$_3$ photocatalyst enable oxygen and hydrogen atom to form S=O and N−H bonds with MB molecule, and then take out two methyl groups to be C$_{14}$H$_{15}$N$_3$OS (m/z = 274) [48,49]. Due to elimination of methyl groups, C$_{14}$H$_{15}$N$_3$OS is degraded to form C$_{12}$H$_{11}$N$_3$OS (m/z = 246). This intermediates product is further degraded to form multiple single ring structures, i.e. C$_8$H$_{13}$NO$_2$ (m/z = 185), C$_8$H$_6$O$_6$ (m/z = 195) and C$_8$H$_{11}$N (m/z = 218). But most of all, C$_8$H$_6$O$_6$ further photodegrades to C$_6$H$_6$O$_4$ (m/z = 149) and later to the formation of C$_5$H8O$_4$ (m/z = 136) which is more easily mineralized than other ring structure intermediates into CO$_2$. It can be seen that the peak at 136 with much higher intensity in 2.7-CaSnO$_3$ than that in 1.0-CaSnO$_3$, indicating that 2.7-CaSnO$_3$ has more efficient photocatalytic performance than 1.0-CaSnO$_3$. In addition, the residual MB over 1.0-CaSnO$_3$ suggests that it does not have enough active sites
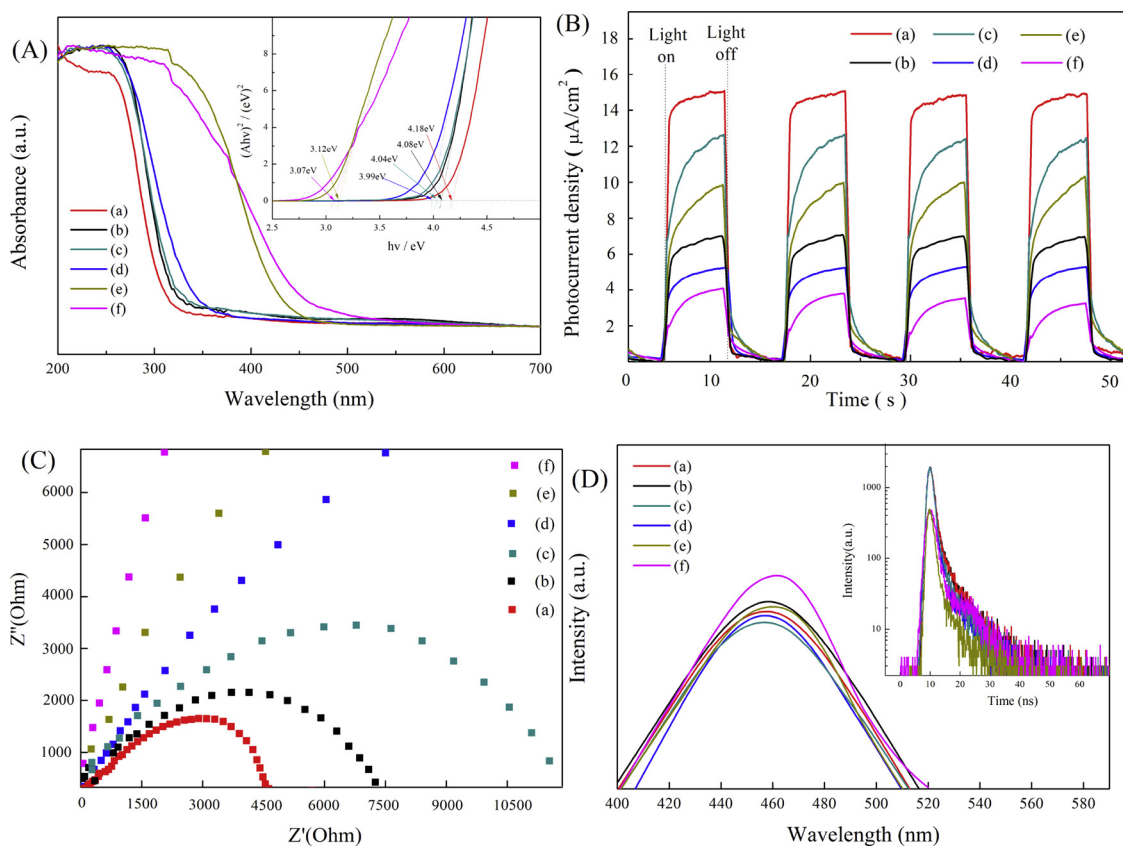

Fig. 7. (A) DRS and inserted ($\alpha h\nu$)^2 as a function of photon energy ($h\nu$); (B) Photocurrent measurements; (C) Nyquist impedance plots; (D) PL spectra with the excitation wavelength of 350 nm and inserted time-resolved PL spectra monitored at 465 nm of (a) 2.7- and (b) 1.0- CaSnO$_3$, (c) 2.3- and (d) 1.0- SrSnO$_3$, (e) 1.7- and (f) 1.0- BaSnO$_3$ samples.
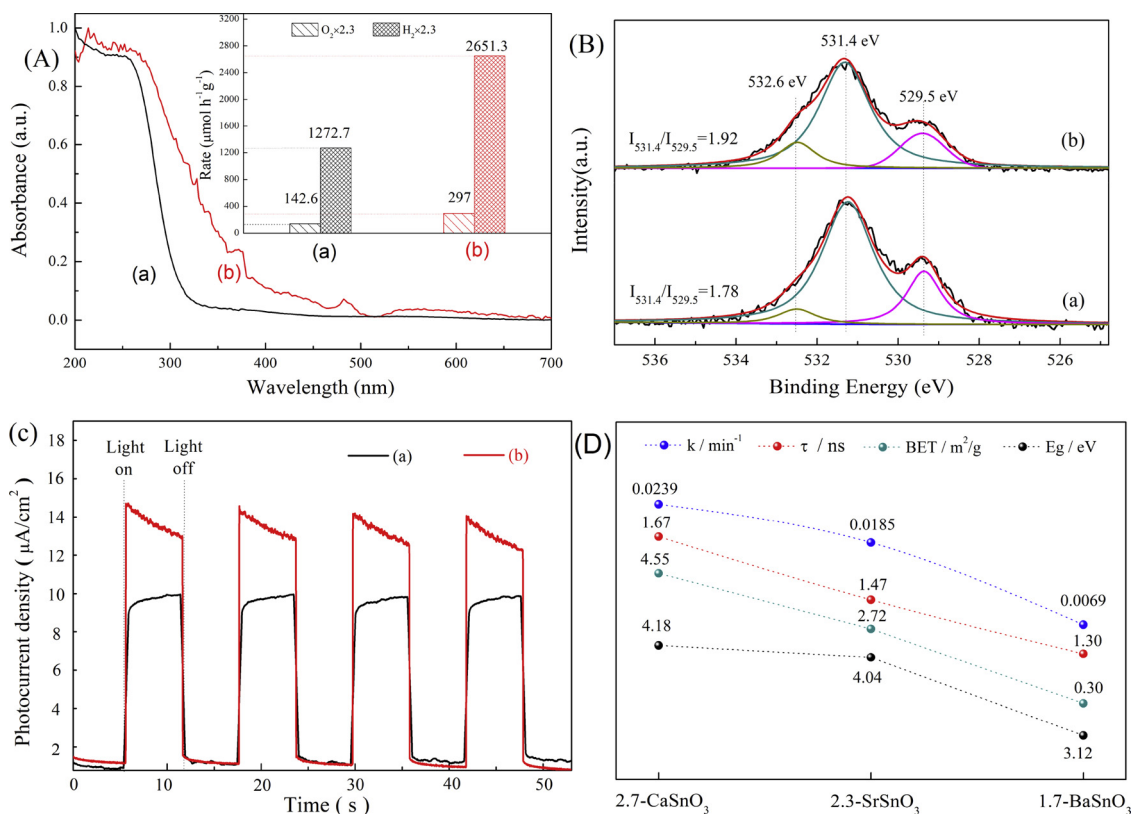
Fig. 8. (A) DRS spectra, and the insert image of O_2 production rates, H_2 production rates, (B) O1 s XPS, and (C) Photocurrent performances of 2.7-CaSnO$_3$ (a) before and (b) after hydrogen gas reduction treatment. (D) Summary of photocatalytic MB degradation rates, PL decay lifetimes, BET specific surface areas, and band gap energy of 2.7-CaSnO$_3$, 2.3-SrSnO$_3$, 1.7-BaSnO$_3$.

to accommodate a lot of MB molecules, on the contrary, oxygen vacancies enable 2.7-CaSnO$_3$ to adsorb more reagent molecules and result in the vanish of 284 amu peak. Therefore, the largest rate constant, the highest degradation and relative simple intermediate products demonstrate the quick decomposition and relative efficient mineralization of MB with the assistance of oxygen vacancies doped 2.7-CaSnO$_3$.

The UV–vis DRS spectra of different MSnO$_3$ photocatalysts are shown in Fig. 7A. The absorption intensity does not increase for all MSnO$_3$. Compared with that of stoichiometric MSnO$_3$, the modified one shows the same absorbance edge, but shift the absorbance to the UV region. The absorption edge extends to the visible region from CaSnO$_3$ to BaSnO$_3$. The band gap energy of 2.7-CaSnO$_3$, 2.3-SrSnO$_3$, 1.7-BaSnO$_3$ are 4.21 eV, 4.05 eV and 3.10 eV respectively. Interestingly enough, a photocatalyst with a larger band gap often has a lower activity, but MSnO$_3$ photocatalysts go beyond that. The 2.7-CaSnO$_3$ samples exhibits much better photocatalytic performance under LED light (Fig. 6A), though its band gap energy is as large as 4.21 eV. It is well known that the activity of the photocatalyst depends on various factors, for example, band gap, crystallinity, lattice defects, surface area, composition, ingredient or surface adsorbents [50]. In this case, the band gap is not the key factor that affects the photocatalytic activity.

As shown in Fig. S6, the relative valence band maximum was speculated via valence band XPS measurement. According to the Kubelka-Munk relation, the band gaps are calculated at 4.21, 4.05 and 3.10 eV for 2.7-CaSnO$_3$, 2.3-SrSnO$_3$, and 1.7-BaSnO$_3$, while 4.08, 3.99, and 3.07 eV for 1.0-CaSnO$_3$, 1.0-SrSnO$_3$, and 1.0-BaSnO$_3$, respectively. Therefore, the valence band (VB) edges and conduction band (CB) edges of 2.7-CaSnO$_3$, 2.3-SrSnO$_3$, and 1.7-BaSnO$_3$ are calculated at 3.04, 3.02, 2.75 and -1.11, -1.02, -0.37 eV, while those for 1.0-CaSnO$_3$, 1.0-SrSnO$_3$, and 1.0-BaSnO$_3$ are 3.01, 2.96, 2.75 and -1.07, -1.03, -0.32 eV, respectively. The band gap results in the electron affinity (CB

edge) and the first ionization energy (VB edge) are similar to those in the other researcher's work [51]. According to the Mott-Schottky plots (Fig. S7), the flat-band potentials are determined to be -0.35, -0.31, -0.37 V for 2.7-CaSnO$_3$, 2.3-SrSnO$_3$, and 1.7-BaSnO$_3$, while -0.40, -0.34, -0.38 V for stoichiometric ones, respectively. All samples should be of n-type characteristics owing to the positive slopes of the linear plots.

Photocurrents are measured for 2.7-CaSnO$_3$, 2.3-SrSnO$_3$, 1.7-BaSnO$_3$ and their stoichiometric samples electrodes to offer information for the separation and transfer efficiency of photogenerated electron and holes (Fig. 7B). All the MSnO$_3$ electrodes show fast and uniform photocurrent responses and reversible photo-responsive phenomenon. Under white LED lamp irradiation, the photocurrents of the M/Sn ratio modified electrodes are higher than that of the stoichiometric ones. The 2.7-CaSnO$_3$ exhibits outstanding performance of photocurrent under the same light irradiation, followed by 2.3-SrSnO$_3$ and 1.7-BaSnO$_3$. The photocurrent enhancement of the ratio modified photocatalyst indicates a limited photogenerated charge carrier recombination, which could be owing to the effect of oxygen defect. In the EIS evaluation (Fig. 7C), according to the semicircle in the low-frequency zone, the charge-transfer resistances of 2.7-CaSnO$_3$, 2.3-SrSnO$_3$, 1.7-BaSnO$_3$ are calculated to 4506, 12403, 20,238 Ω, and those of their stoichiometric samples are 7143, 17399, 25,721 Ω, indicating that 2.7-CaSnO$_3$ has a faster charge transfer rate.

The PL decay is studied by time-resolved spectra. As can be seen in the insert spectra in Fig. 7D, 2.7-CaSnO$_3$ has a longer lifetime, indicating a slower charge recombination. Since the decay curves are fitted to the one-exponential function, the average lifetimes of the entire decay are calculated to be 1.67, 1.47, 1.30 ns for 2.7-CaSnO$_3$, 2.3-SrSnO$_3$, 1.7-BaSnO$_3$ respectively. In addition, the PL spectra analysis is used to further study the recombination rate of photo-generated carriers. As shown in Fig. 7D and Fig. S8a-c, all modified MSnO$_3$ samples exhibit weaker PL intensity than their own stoichiometric one,

suggesting the slower recombination of electrons and holes.

To further investigate the effect of oxygen vacancy on the performance of $MSnO_3$ photocatalyst, the 2.7-$CaSnO_3$ was treated by hydrogen gas reduction. Hydrogen reduction treatment should benefit the formation of more oxygen vacancies [52]. As shown in XRD patterns in Fig. S9, after hydrogen gas treatment, the impurity peaks of Ca_3SnO become more obvious. The absorption edge of 2.7-$CaSnO_3$ sample redshift and improved visible light responsive ability can be attributed to the hydrogen destroy the surface of it at high temperature as shown in Fig. 8A. The red-shift of the absorption wavelength indicates that the oxygen vacancy rich $CaSnO_3$ can absorb more photons. In O1 s XPS spectrum (Fig. 8B), the intensity of the O 1 s peak at 531.4 eV increases while that at 529.5 eV decreases after hydrogen treatment, demonstrate the increasing of the oxygen vacancy or defect and the decreasing of the lattice oxygen in the $CaSnO_3$. Therefore, as can be seen in the insert image in Fig. 8A, not only the O_2 but also the H_2 production rate of 2.7-$CaSnO_3$ is improved after hydrogen gas reduction treatment. Furthermore, after hydrogen reduction, the photocurrent response of 2.7-$CaSnO_3$ is also improved, indicating more charge carriers transfer, as shown in Fig. 8C. In summary, as shown in Fig. 8D, the different factors affected by vacancy or defect in three $MSnO_3$ sample are investigated. Compared with 2.3-$SrSnO_3$ and 1.7-$BaSnO_3$, 2.7-$CaSnO_3$ possesses higher specific surface area and longer excited electron life therefore better photocatalytic performance, though its band gap energy is large. As a $MSnO_3$ photocatalyst, 1.7-$BaSnO_3$ does not show improved performance after nonstoichiometric preparation.

Therefore, as a summary listed in Table 1, introducing defects of O vacancies in $CaSnO_3$ through a nonstoichiometric strategy can improve its photocatalytic performance and accelerate the superoxide radical production. Thanks to the unsaturated sites in 2.7-$CaSnO_3$, the electrons can transfer more freely and also benefit for molecular adsorption. The characteristic electronic and defective structures enable the 2.7-$CaSnO_3$ to have unique physical and chemical properties, which include the improved electron transfer, selective adsorption, and high photocatalytic properties. The O vacancies in the 2.7-$CaSnO_3$ will promote the selective adsorption of the reactant molecule and drive the further reactions at a molecular level.

4. Conclusion

In summary, the oxygen vacancies on $MSnO_3$ with numerous unsaturated sites on the surface for oxygen activation have been created and controlled. By transferring charge carriers to the chemisorbed oxygen, the defect sites realize the energy coupling of excitons with oxygen species. The formed superoxide radicals in a chemisorbed state can drive the O_2-pariciping photocatalytic reaction. Therefore, the modified $MSnO_3$ photocatalysts show efficiently enhanced photocatalytic activity. Especially, 2.7-$CaSnO_3$ exhibits outstanding performance on photogenerated electrons and holes separation and energy transfer. This work should provide a guideline for the design of highly efficient photocatalysts towards oxygen-participating catalytic reaction by inducing oxygen vacancies in photocatalysts.

Appendix A. Supplementary data

Supplementary material related to this article can be found, in the online version, at doi:https://doi.org/10.1016/j.apcatb.2018.10.076.

References

[1] S. MiarAlipour, D. Friedmann, J. Scott, R. Amal, J. Hazard. Mater. 341 (2018) 404–423.

[2] H.L. Tan, R. Amal, Y.H. Ng, J. Mater. Chem. A Mater. Energy Sustain. 5 (2017) 16498–16521.

[3] Ch.H. An, Sh.T. Wang, Y.G. Sun, Q.H. Zhang, J. Zhang, Ch.Y. Wang, J.Y. Fang, J. Mater. Chem. A 4 (2016) 4336–4352.

[4] D. Pan, S.H.S. Ge, X.Y. Zhang, X.M. Mai, S.H.Y. Li, Z.H. Guo, Dalton Trans. 47 (2018) 708–715.

[5] M.B. Gawande, A. Goswami, F.X. Felpin, T. Asefa, X.X. Huang, R. Silva, X.X. Zou, R. Zboril, R.S. Varma, Chem. Rev. 116 (2016) 3722–3811.

[6] R.Q. Ye, H.B. Fang, Y.Z. Zheng, N. Li, Y. Wang, X. Tao, ACS. Appl. Mater. Interface 8 (2016) 13879–13889.

[7] W.F. Zhang, J.W. Tang, J.H. Ye, J. Mater. Res. 22 (2007) 1859–1871.

[8] W. Wang, M.O. Tade, Z.P. Shao, Prog. Mater. Sci. 92 (2018) 33–63.

[9] J.X. Low, J.G. Yu, M. Jaroniec, S. Wageh, A.A. Al-Ghamdi, Adv. Mater. 29 (2017) 1601694.

[10] N. Zhang, X.Y. Li, H.C. Ye, S.M. Chen, H.X. Ju, D.B. Liu, Y. Lin, W. Ye, C.G. Wang, Q. Xu, J.F. Zhu, L. Song, J. Jiang, Y.J. Xiong, J. Am. Chem. Soc. 138 (2016) 8928–8935.

[11] H. Li, J. Li, Z.H. Ai, F.L. Jia, L.Z. Zhang, Angew. Chem. Int. Ed. 58 (2018) 122–138.

[12] H. Hirakawa, M. Hashimoto, Y. Shiraishi, T. Hirai, J. Am. Chem. Soc. 139 (2017) 10929–10936.

[13] S.Y. Wang, X. Hai, X. Ding, K. Chang, Y.G. Xiang, X.G. Meng, Z.X. Yang, H. Chen, J.H. Ye, Adv. Mater. 29 (2017) 1701774.

[14] X.B. Fan, S. Yu, F. Zhan, Z.J. Li, Y.J. Gao, X.B. Li, L.P. Zhang, Y. Tao, C.H. Tung, L.Z. Wu, ChemSusChem 10 (2017) 4833–4838.

[15] W.K. Wang, M. Gao, X. Zhang, M. Fujitsuka, T. Majima, H.Q. Yu, Appl. Catal. B: Environ. 205 (2017) 165–172.

[16] M.C. Long, P.D. Hu, H.D. Wu, J. Cai, B.H. Tan, B.X. Zhou, Appl. Catal. B: Environ. 184 (2016) 20–27.

[17] J.N. Hui, G. Zhang, C.S. Ni, J.T.S. Irvine, Chem. Commun. (Camb.) 53 (2017) 10038–10041.

[18] T. Alammar, I. Hamm, V. Grasmik, M. Wark, A.V. Mudring, Inorg. Chem. 56 (2017) 6920–6932.

[19] W. Gao, W.Y. Zhang, G.X. Lu, Appl. Catal. B: Environ. 212 (2017) 23–31.

[20] W.J. Wang, S.J. Liang, K.N. Ding, J.H. Bi, J.C. Yu, P.K.Wong.L. Wu, J. Mater. Sci. 49 (2014) 1893–1902.

[21] H. Einaga, Y. Nasu, M. Oda, H. Saito, Chem. Eng. J. 283 (2016) 97–104.

[22] J.Y. Chen, Z.G. He, G.Y. Li, T.C. An, H.X. Shi, Y.Z. Li, Appl. Catal. B: Environ. 209 (2017) 146–154.

[23] Q. Zhang, Y. Huang, S.Q. Peng, Y.F. Zhang, Z.X. Shen, J.J. Cao, W.K. Ho, S.C. Lee, D.Y.H. Pui, Appl. Catal. B: Environ. 204 (2017) 346–357.

[24] G.Q. Zhang, S.R. Sun, W.S. Jiang, X. Miao, Z. Zhao, X.Y. Zhang, D. Qu, D.Y. Zhang, D.B. Li, Z.C. Sun, Adv. Energy Mater. (2016) 1600932.

[25] J.J. Shan, F. Raziq, M. Humayun, W. Zhou, Y. Qu, G.F. Wang, Y.D. Li, Appl. Catal. B: Environ. 219 (2017) 10–17.

[26] X. Sun, D. Jiang, L. Zhang, S.M. Sun, W.Z. Wang, ACS Sustainable Chem. Eng. 5 (2017) 9965–9971.

[27] Q.L. Yang, G.L. Liu, Y. Liu, Ind. Eng. Chem. Res. 57 (2018) 1–17.

[28] J. Hwang, R. Rao, L. Giordano, Y. Katayama, Y. Yu, Y. Shao-Horn, Science 358 (2017) 751–756.

[29] K.F. Zhang, Y.X. Liu, J.G. Deng, S.H. Xie, X.T. Zhao, J. Yang, Z. Han, H.X. Dai, Appl. Catal. B: Environ. 224 (2018) 350–359.

[30] H.Q. Tan, Z. Zhao, W.B. Zhu, E.N. Coker, B.S. Li, M. Zheng, W.X. Yu, Y. Fan, Z.C. Sun, ACS Appl. Mater. Interfaces 6 (2014) 19184–19190.

[31] H. Li, H. Zhou, Z.Z. Zhuo, G.L. Wei, X. Zhuang, S.W. Zhong, X.N. Deng, J.G. Li, Wang, J. Mater. Chem. A 6 (2018) 2264–2272.

[32] F.L. Zhong, H.Q. Zhuang, Q. Gu, J.L. Long, RSC Adv. 6 (2016) 42474–42481.

[33] K. Ridier, D. Aureau, B. Bérini, Y. Dumont, N. Keller, J. Vigneron, A. Etcheberry, B. Domengès, A. Fouchet, Phys. Rev. B 97 (2018) 035146.

[34] S.B. Hammouda, F.P. Zhao, Z. Safae, V. Srivastava, D.L. Ramasamy, S. Iftekhar, S. Kalliola, M. Sillanpää, Appl. Catal. B: Environ. 215 (2017) 60–73.

[35] P. Sangaiya, R. Jayaprakash, Mat. Sci. Semicon. Proc. 85 (2018) 40–51.

[36] J.D. Xiao, J. Rabeah, J. Yang, Y.B. Xie, H.B. Cao, A. Bruckner, ACS Catal. 7 (2017) 6198–6206.

[37] O.V. Ovchinnikov, A.V. Evtukhova, T.S. Kondratenko, M.S. Smirnov, V.Y. Khokhlov, O.V. Erina, Vib. Spectrosc. 86 (2016) 181–189.

[38] W.J. Ji, R.Q. Hao, W.W. Pei, L. Feng, Q.G. Zhai, Dalton Trans. 47 (2018) 700–707.

[39] G.L. Lucena, L.C. Lima, L.M.C. Honório, A.L.M. Oliveira, R.L. Tranquilim, E. Longo, A.G. Souza, A.S. Maia, I.M.G. Santos, Cermica 63 (2017) 536–541.

[40] T. Alammar, I. Hamm, Viktoria Grasmik, M. Wark, A.V. Mudring, Inorg. Chem. 56 (2018) 6920–6932.

[41] S. Moshtaghi, S. Zinatloo-Ajabshir, M. Salavati-Niasari, J Mater Sci: Mater Electron. 27 (2016) 834–842.

[42] Y. Wang, R. Shi, J. Lin, Y. Zhu, Energy Environ. Sci. 4 (2011) 2922–2929.

[43] M.K. Li, Z.M. Qiang, C. Pulgarin, J. Kiwi, Appl. Catal. B: Environ. 187 (2016) 83–89.

[44] a) O. SakinOmer, M.A. Hussein, B.H.M. Hussein, ArbiMgaidi, Arab. J. Chem 11 (2018) 615–623;
b) Y. Liu, X. Liu, Y. Zhao, D.D. Dionysiou, Appl. Catal. B: Environ. 213 (2017) 74–86.

[45] J.C. He, J. Li, W. Du, Q.X. Han, Z.L. Wang, M.X. Li, J. Alloys Compd. 750 (2018) 360–367.

[46] L.H. Hu, J.X. Zhang, N. Li, S.D. Zhang, F. Chen, B. Ji, H.F. Li, Z.Y. Wang, J. Chem. Technol. Biot. 93 (2018) 2208–2215.

[47] Y.X. Zhang, M.J. Xu, H. Li, H. Ge, Z.F. Bian, Appl. Catal. B: Environ. 226 (2018) 213–219.

[48] S.K. Ray, D. Dhakal, Y.K. Kshetri, S.W. Lee, J. Photochem. Photobiol. A: Chem. 348

(2017) 18–32.

[49] R.G. Nair, S. Mazumdar, B. Modak, R. Bapat, P. Ayyub, K. Bhattacharyya, J. Photochem. Photobiol. A: Chem. 345 (2017) 36–53.

[50] G.R. Bertolini, L.R. Pizzio, A. Kubacka, M.J. Muñoz-Batista, M. Fernández-García, Appl. Catal. B: Environ. 225 (2018) 100–109.

[51] J. Liu, Y. Liu, N.Y. Liu, Y.Z. Han, X. Zhang, H. Huang, Y. Lifshitz, S.T. Lee, J. Zhong, Z.H. Kang, Science 347 (2015) 970–974.

[52] J.W. Li, B. Wei, Z.Q. Cao, X. Yue, Y.X. Zhang, Z. Lu, ChemSusChem 11 (2018) 254–263.